Noise, sampling, and the number of projections in cone-beam CT with a flat-panel detector

Z. Zhao
Department of Biomedical Engineering, Johns Hopkins University, Baltimore, Maryland 21205 and Department of Biomedical Engineering, Tianjin University, Tianjin, China 300072

G. J. Gang
Department of Biomedical Engineering, Johns Hopkins University, Baltimore, Maryland 21205 and Institute of Biomaterials and Biomedical Engineering, University of Toronto, Toronto, Ontario M5G 2M9, Canada

J. H. Siewerdsen[a)]
Department of Biomedical Engineering, Johns Hopkins University, Baltimore, Maryland 21205; Institute of Biomaterials and Biomedical Engineering, University of Toronto, Toronto, Ontario M5G 2M9, Canada; Department of Computer Science, Johns Hopkins University, Baltimore, Maryland 21205; and Russell H. Morgan Department of Radiology, Johns Hopkins University, Baltimore, Maryland 21205

(Received 26 September 2013; revised 17 April 2014; accepted for publication 22 April 2014; published 20 May 2014)

Purpose: To investigate the effect of the number of projection views on image noise in cone-beam CT (CBCT) with a flat-panel detector.
Methods: This fairly fundamental consideration in CBCT system design and operation was addressed experimentally (using a phantom presenting a uniform medium as well as statistically motivated "clutter") and theoretically (using a cascaded systems model describing CBCT noise) to elucidate the contributing factors of quantum noise (σ_Q), electronic noise (σ_E), and view aliasing (σ_{view}). Analysis included investigation of the noise, noise-power spectrum, and modulation transfer function as a function of the number of projections (N_{proj}), dose (D_{tot}), and voxel size (b_{vox}).
Results: The results reveal a nonmonotonic relationship between image noise and N_{proj} at fixed total dose: for the CBCT system considered, noise decreased with increasing N_{proj} due to reduction of view sampling effects in the regime $N_{\text{proj}} <\sim 200$, above which noise increased with N_{proj} due to increased electronic noise. View sampling effects were shown to depend on the heterogeneity of the object in a direct analytical relationship to power-law anatomical clutter of the form κ/f^{β}—and a general model of individual noise components (σ_Q, σ_E, and σ_{view}) demonstrated agreement with measurements over a broad range in N_{proj}, D_{tot}, and b_{vox}.
Conclusions: The work elucidates fairly basic elements of CBCT noise in a manner that demonstrates the role of distinct noise components (viz., quantum, electronic, and view sampling noise). For configurations fairly typical of CBCT with a flat-panel detector (FPD), the analysis reveals a "sweet spot" (i.e., minimum noise) in the range $N_{proj} \sim 250$–350, nearly an order of magnitude lower in N_{proj} than typical of multidetector CT, owing to the relatively high electronic noise in FPDs. The analysis explicitly relates view aliasing and quantum noise in a manner that includes aspects of the object ("clutter") and imaging chain (including nonidealities of detector blur and electronic noise) to provide a more rigorous basis for commonly held intuition and heurism in CBCT system design and operation.
© *2014 American Association of Physicists in Medicine*. [http://dx.doi.org/10.1118/1.4875688]

Key words: cone-beam CT, quantum noise, electronic noise, view-sampling, cascaded systems analysis, image quality

1. INTRODUCTION

Among the first questions encountered in developing a new cone-beam CT (CBCT) system is: How many projections should be acquired? The question is inextricably linked to factors of radiation dose, acquisition speed, data handling, and—of course—image quality. With respect to the last, a simple rule of thumb might be invoked: Acquire at least a number of projections (N_{proj}) such that the angular separation between views ($\Delta\theta$) amounts to a distance at the edge of the field of view (FOV) equal to the voxel size (b_{vox})

$$N_{\text{proj}} \geq 2\pi / \arctan(2b_{\text{vox}}/\text{FOV}), \quad (1)$$

where for simplicity, we assume a full circular orbit ($N_{\text{proj}}\Delta\theta = 2\pi$). One could (in fact, should) invoke a measure of spatial resolution or characteristic correlation length that is distinct from the voxel size—for example, the full-width at half maximum of the point-spread function; however, the simple rule of thumb in Eq. (1) essentially assumes voxel size as a coarse surrogate. Along similar lines, one could more strictly invoke the Nyquist theorem in that the sampling distance should be no more than half the desired resolution distance, requiring $b_{\text{vox}} \rightarrow b_{\text{vox}}/2$. While Eq. (1) is obviously an oversimplification with respect to numerous factors detailed below, it is not an unreasonable starting point. Why then, does the answer imply something so different from what is typically

implemented in CBCT? For example, a CBCT scanner with FOV ~250 mm and a desired spatial resolution of 0.5 mm would imply N_{proj} ~1500 (and $\Delta\theta$ ~0.23°). The variation with $b_{vox} \rightarrow b_{vox}/2$ implies N_{proj} ~3100. These numbers are not unlike the number of projections acquired in fan-beam multidetector diagnostic CT, but in CBCT—in applications ranging from diagnostic imaging of the breast,[1,2] extremities,[3] and head[4] to image-guided surgery[5,6] and radiotherapy[7]—acquisition more typically involves N_{proj} ~350–450 (with $\Delta\theta$ ~0.8°–1°). What accounts for the factor of ~3–8 between such real CBCT embodiments and the answer implied by the (overly simplistic) Eq. (1)? And would CBCT image quality improve by increasing N_{proj} several-fold, assuming other factors such as readout speed and radiation dose could be held fixed?

An experienced practitioner of CBCT would likely answer confidently—*No*—and a number of reasons for the lower N_{proj} in CBCT could immediately be offered. For example: (1) Flat-panel detectors (FPDs) have a high level of electronic noise; therefore, increasing N_{proj} (at fixed dose) would entail a lower exposure per projection and an unacceptably high contribution of electronic noise; (2) Indirect-detection FPDs have blur associated the x-ray converter that exceeds the voxel size; therefore, b_{vox} in Eq. (1) can be replaced by a larger correlation length, giving a smaller N_{proj}; and (3) FPDs have relatively slow frame rate, so increasing N_{proj} would entail unacceptably long scan times and potential for motion artifact. Such empirical rationale—and the conditions under which such rationale fails—are given a more rigorous analytical basis in this paper, including aspects of anatomical clutter, detector nonidealities, and view sampling. The effects of sampling and aliasing in CT have been described in early work by Brooks *et al.*[8] and Joseph *et al.*,[9,10] providing insight far beyond that of Eq. (1). Such effects are considered here in the context of CBCT with FPDs (which exhibit less idealized performance with respect to detector blur and electronic noise) and cascaded systems analysis of 3D signal and noise transfer characteristics.

We entertained the question first by way of a simple experiment. A phantom presenting uniform and heterogeneous content was used to measure CBCT image noise as a function of N_{proj} at fixed total scan dose. The observations were subsequently interpreted using a cascaded systems model[11,12] for signal and noise propagation to elucidate the theoretical underpinnings of quantum noise, electronic noise, anatomical clutter, and view sampling effects as a function of N_{proj}. While previous work has demonstrated the dependence of CBCT imaging performance on factors such as dose, reconstruction parameters, anatomical noise, and the imaging task,[11–19] the current work sheds light on the behavior of CBCT image noise with specific regard to view sampling and a finite number of views. It also reveals a new and nontrivial relationship between view sampling and anatomical clutter and demonstrates why the choice of N_{proj} ~350–450 for the current generation of CBCT systems is not only a reasonable, practical choice (e.g., in terms of scan time), it is in several respects optimal in minimizing the combined influence of quantum noise, electronics noise, and view aliasing for a typical system configuration.

2. EXPERIMENTAL METHODS

2.A. Imaging bench, techniques, and phantom

All experiments were conducted using the CBCT imaging bench in Fig. 1(a). The bench consisted of an x-ray source [DU694 pulsed radiographic/fluoroscopic tube in EA10 housing, Dunlee, Aurora IL], FPD [PaxScan 4343, Varian Medical Systems, Palo Alto, CA], and a computer-controlled motion system: seven linear stages [406XR and HLE60SR linear stages, Parker Hannifin, Cleveland OH] to set overall system geometry and a rotation stage [Dynaserv G3 servo drive, Parker Hannifin, Cleveland, OH)] to rotate the object. The system was operated in a step-and-shoot mode in which the x-ray source delivers pulsed fluoroscopy (typically 10 ms pulses), the FPD is read (typically 3 fps), and the object rotates (e.g., by an angular increment $\Delta\theta$) in a synchronized manner. The FPD was read at a nominal pixel size of 0.278 mm (referred to as 1 × 1 binning) or 0.556 mm (2 × 2 binning). The system geometry for all experiments entailed source-axis distance (SAD) = 1225 mm and source-detector distance = 1502 mm, calibrated using the two-circle BB phantom method described by Cho *et al.*[20] An antiscatter grid was attached to the FPD (10:1 grid ratio, 103 lpi, and measured transmission factor 0.55, Soyee Products, Korea). A set of 50 dark images and 50 flood images

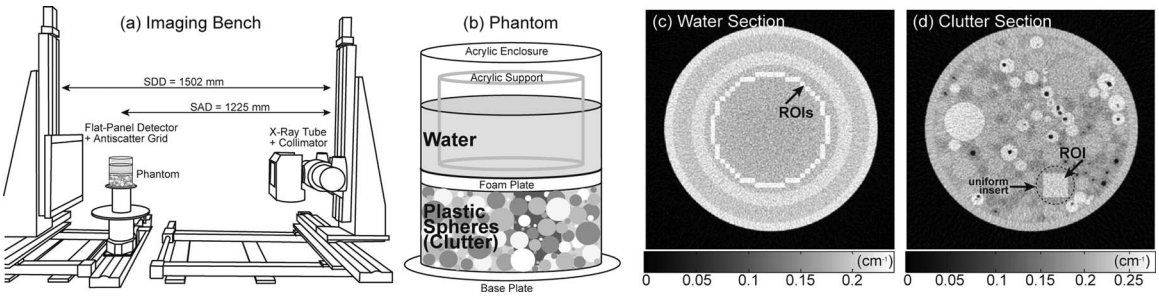

FIG. 1. Imaging bench and phantom. (a) Illustration of the x-ray imaging bench, components, and system geometry. (b) Illustration of the cylindrical phantom with water (top) and a heterogeneous mixture of plastic spheres (bottom). (c) Example CBCT axial slices of the phantom. The water region included an acrylic annulus as part of the phantom construction, and the small white squares superimposed at constant radius mark the location of ROIs for noise analysis. The spherical clutter region included three electron-density inserts (larger circles at 1, 5, and 9 o'clock positions), and the white square superimposed in the low-density insert shows the location of the ROI for noise analysis.

TABLE I. Summary of CBCT acquisition techniques giving constant nominal dose (D_{tot} = 2 or 8 mGy) for various settings of number of projections (N_{proj}) and exposure per projection (X_{proj}) in air at isocenter (SAD = 1225 mm). Careful adjustment of N_{proj} and X_{proj} yielded constant D_{tot} within 1% for all experiments.

Nominal D_{tot} (mGy)	N_{proj}	mAs/proj	Measured X_{proj} (mR)	Measured X_{tot} (mR)	Estimated D_{tot} (mGy)	%err
2	40	5.00	5.17	206.80	2.01	0.72
2	80	2.50	2.59	207.20	2.02	0.91
2	159	1.25	1.30	206.70	2.01	0.67
2	308	0.63	0.67	206.36	2.01	0.50
2	480	0.40	0.43	206.40	2.01	0.52
2	736	0.25	0.28	206.08	2.01	0.37
2	1085	0.16	0.19	206.15	2.01	0.40
2	1375	0.13	0.15	206.25	2.01	0.45
8	160	5.00	5.17	827.20	8.06	0.72
8	213	4.00	3.88	826.44	8.05	0.63
8	318	2.50	2.59	823.62	8.02	0.28
8	488	1.60	1.69	824.72	8.03	0.42
8	634	1.25	1.30	824.20	8.03	0.35
8	959	0.80	0.86	824.74	8.03	0.42
8	1231	0.63	0.67	824.77	8.03	0.42

acquired before or after each scan provided correction of pixel offset and gain variations. Image reconstruction was based on 3D filtered backprojection adapted from Feldkamp *et al.*,[21] and all scans involved a complete 360° rotation of the object. Reconstructions were performed at isotropic voxel size $b_x = b_y = b_z = 0.22$ mm (for 1 × 1 binning of the FPD) and 0.44 mm (for 2 × 2 binning).

All scans were performed at 90 kVp (+2 mm Al +0.4 mm Cu added filtration). Beam quality estimated by Spektr[22] indicated half-value layer (HVL) = 7.9 mm Al, mean energy = 59.2 keV, and 1.53 mR/mAs at a distance of 1000 mm from the source. Bare-beam exposure was measured (at isocenter and at the surface of the antiscatter grid) using a silicon diode (DDX6-W, Radcal, Monrovia, CA) and exposure meter (Accu-Pro 9096, Radcal, Monrovia, CA). The measured mR/mAs agreed with the Spektr calculation to better than 1%. Dose was measured using a 0.6 cm^3 Farmer ionization chamber placed at the center of a 16 cm CTDI phantom at isocenter (with the phantom extended longitudinally above and below by a stack of two additional CTDI phantoms). The scan dose (D_{tot}) and exposure per projection (X_{proj} in air at isocenter) can be related by

$$D_{tot} = N_{proj} \cdot X_{proj} \cdot e^{-\mu D/2} \cdot f \cdot f_{BSF}, \quad (2)$$

where μ was the effective attenuation coefficient of water for the 90 kVp spectrum (0.019 mm^{-1}), D was the diameter of the phantom (15.5 cm as described below), the f factor was taken as 0.9 cGy/R, and the backscatter factor (f_{BSF}) was empirically determined to be ~4.5 such that the measured dose and exposure were in close agreement (better than 5%) according to Eq. (2).

As detailed in Table I, experiments were conducted at two nominal dose levels, D_{tot} = 2 and 8 mGy. CBCT scans were acquired at fixed total dose by careful variation of the number of projections (N_{proj} ranging 40–1375) and the mAs/projection (ranging 5–0.126 mAs per projection, giving exposure per projection X_{proj} = 0.15–5.17 mR). Note that the highest mAs did not saturate the FPD (5 mAs giving ~75% of sensor saturation) such that all measurements were within a linear regime of detector response. These settings provided total dose as calculated by Eq. (2) within 1% of the nominal dose level for all cases, as shown in Table I. The experiments therefore spanned more than an order of magnitude in detector exposure, with the intention of varying the influence of electronic noise from a negligible level (high X_{proj}) to a more appreciable level (low X_{proj}) all at fixed total dose.

A phantom was constructed to elucidate the influence of various components of CBCT image noise—viz., quantum noise, electronic noise, anatomical clutter, and view aliasing—as a function of the total scan dose (D_{tot}), the number of projections (N_{proj}), and reconstruction voxel size (isotropic b_{vox}). The phantom is illustrated in Fig. 1, based on a 15 cm diameter plastic cylinder in which two "layers" of material were incorporated (separated by a foam disk). The top layer was water, and the bottom was a mixed collection of plastic spheres of varying diameter (1.6–12.7 mm) and material type (polypropylene, acrylic, and acetal) in water. Such a random assembly of self-similar objects was shown previously[12] to constitute a fractal described by a ~$1/f^3$ power-law distribution similar to that measured for anatomical noise-power spectra ("anatomical clutter") in contexts such as breast[23,24] and chest imaging.[25,26] The contrast of the spheres (i.e., the amplitude of the simulated anatomical clutter) was chosen to approximate that typical of natural tissues (e.g., polypropylene and acrylic representing soft tissues with ~100 HU contrast to water and acetal representing bone at several hundred HU contrast). The phantom was thus statistically motivated such that the top layer presented stochastic quantum and electronic noise only, and the bottom presented a combination of stochastic noise and anatomical clutter. Three tissue-simulating, cylindrical electron density inserts [$\rho_e^w \approx 0.96$ (Breast), $\rho_e^w \approx 1.07$ (Liver), and $\rho_e^w \approx 1.10$ (B-200, Bone); Gammex RMI, Madison WI] were also incorporated in the bottom layer for analysis of contrast and noise.

2.B. Analysis of noise

The experiment permitted analysis of various components of CBCT image noise (i.e., quantum, electronic, anatomical, and view aliasing noise) in terms of the standard deviation in voxel values (σ_{vox}), and analysis of the noise-power spectrum (NPS) gave additional insight on the spatial frequency content of such noise components. The regions of interest (ROIs) for noise and NPS analysis are illustrated in Fig. 1. In each case, ROIs were within ~3 cm of the central axial slice (cone angle $<1.5^\circ$ for the geometry in Fig. 1), so the effects of the frequency domain "null cone" associated with violation of Tuy's condition for a circular source-detector orbit were considered negligible. Each ROI comprised a 3D cubic subvolume (not a 2D square implied by the slice images in Fig. 1) of sidelength $N_x = N_y = N_z$, with the size and number of ROIs varied as follows.

For analysis of (i) voxel noise and (ii) NPS associated with the purely stochastic effects of x-ray quantum noise and readout electronics noise, the ROIs were placed at a fixed radius (~4 cm) in the water section as in Fig. 1(c). For analysis of (i) voxel noise, the standard deviation was analyzed in ROIs of size $N_x = 16$, giving a total of 512 ROIs in eight contiguous, nonoverlapping slabs within 3 cm of the central axial slice. For analysis of (ii) the NPS, two identical CBCT scans were acquired in succession and subtracted. The NPS was computed from the resulting difference image by discrete Fourier transform in ROIs of size $N_x = 64$, giving a total of 24 nonoverlapping ROIs, correcting by a factor of 2 to account for the subtraction

$$NPS = \frac{1}{2}\frac{b_x b_y b_z}{N_x N_y N_z}\langle |FT[\Delta ROI(x,y,z)]|^2\rangle, \quad (3)$$

where the $\langle . \rangle$ bracket notation represents ensemble average of the NPS estimate from each ROI. The ROIs were not rotated or resampled prior to Fourier transform, so the analysis tended to average out underlying azimuthal angular dependence in the NPS. In each case shown in Table I, the voxel noise was verified to agree with the volume of the NPS to within ~2%.

For analysis of (iii) the voxel noise associated with the combined effects of view sampling and stochastic quantum and electronic noise, the standard deviation was analyzed in a single ROI of size ($80 \times 80 \times 80$) voxels placed in an otherwise uniform region of the solid water insert in the clutter section as in Fig. 1(d). Since the ROI was surrounded by heterogeneous clutter, the standard deviation measured within the otherwise uniform ROI probed a combination of stochastic noise and view aliasing "streaks" from surrounding structures.

3. EXPERIMENTAL RESULTS

Figure 2 illustrates the central experimental result, showing axial reconstructions of the water layer, the clutter layer, and the associated axial and coronal NPS. Results are shown for the case $D_{tot} = 2$ mGy and reconstruction at isotropic voxel size $b_{vox} = b_x = b_y = b_z = 0.22$ mm (1×1 binning). Other image examples [$D_{tot} = 8$ mGy and $b_{vox} = 0.44$ mm (i.e., 2×2 binning)] are not shown but are discussed below.

A naïve guess at the behavior of noise versus N_{proj} might be that since D_{tot} is fixed, the noise should be constant; of course, that refers only to the quantum noise component, and Fig. 2 reveals a far richer mix of contributing noise factors. Close inspection reveals a change in both the magnitude and frequency content of noise as a function of N_{proj}. At the lowest N_{proj}, the noise in water changes only slightly, and there is little or no change in spatial frequency content; however, the noise in the clutter layer increases markedly and demonstrates a dramatic change in spatial frequency content—namely, streaks. The observation points to a conclusion that is clear in retrospect: as the number of

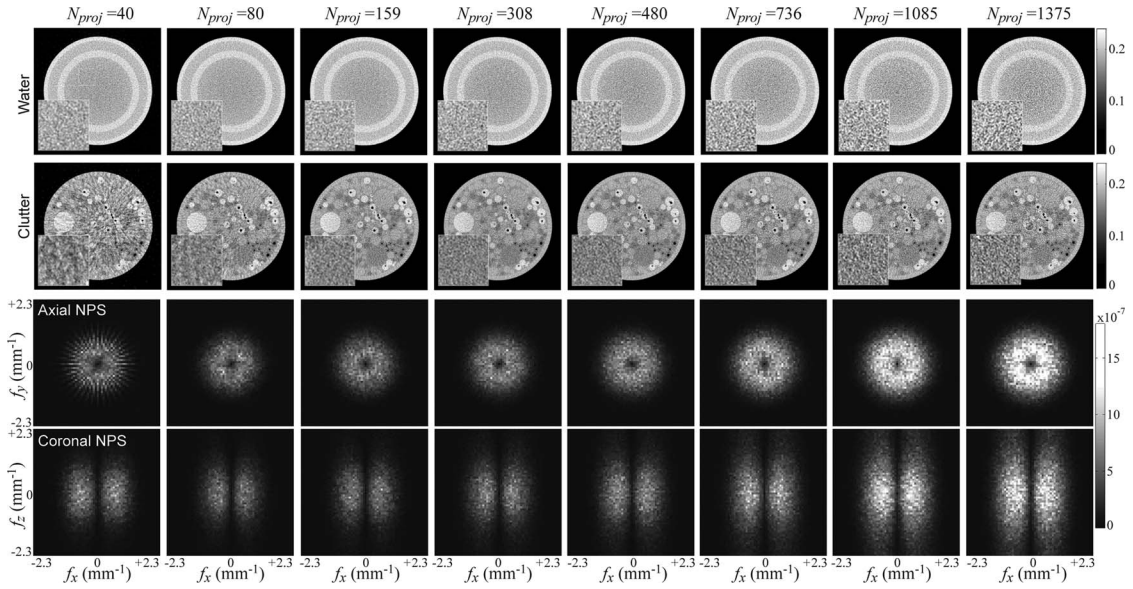

FIG. 2. Images and NPS as a function of N_{proj}. (First row) Axial images in the uniform water region. (Second row) Axial images in the heterogenous clutter region. Zoomed insets illustrate the magnitude and texture of noise as a function of N_{proj}. (Third row) Axial and (fourth row) coronal NPS analyzed in the uniform water region.

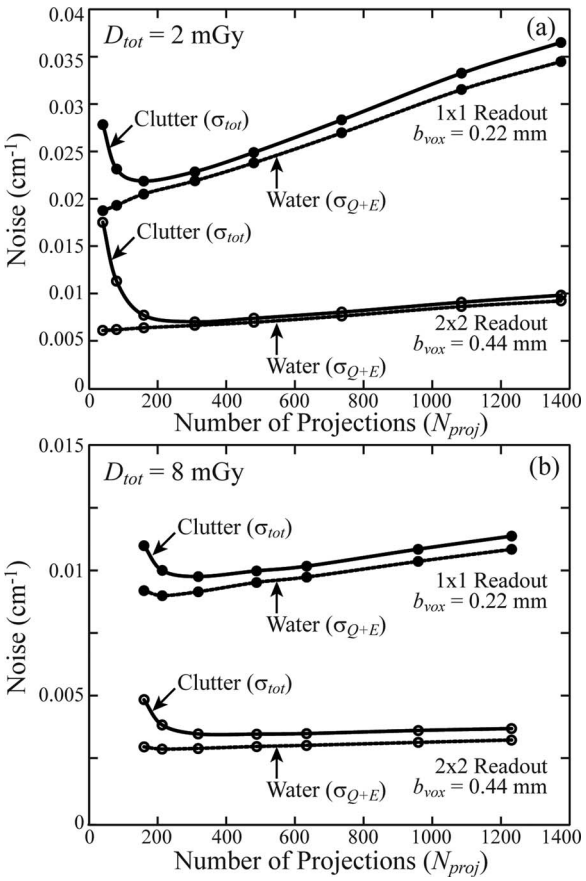

FIG. 3. Voxel noise measured as function of N_{proj} for 3D image reconstructions at (a) $D_{\text{tot}} = 2$ and (b) $D_{\text{tot}} = 8$ mGy.

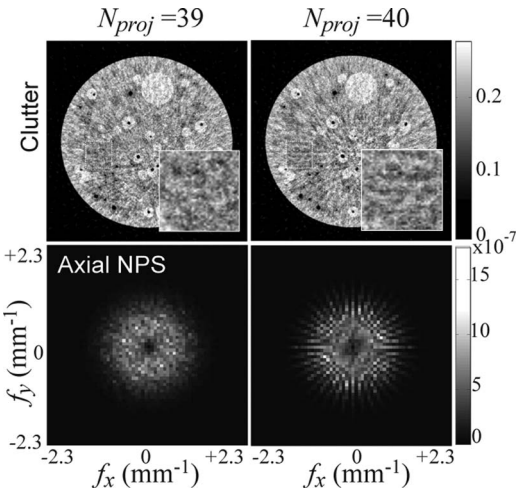

FIG. 4. Images and NPS for $N_{\text{proj}} = 39$ and 40. The latter case results in redundant views and nearly overlapping backprojections with poorer filling of the Fourier domain and correspondingly increased view sampling effects. The former case reduces such view sampling effects (despite having one fewer projection).

projections is reduced, the dominant change in noise characteristic is view sampling that can be well appreciated within a heterogeneous context (clutter) but is not evident in a uniform medium (water). A simple CNR phantom (typically involving a few inserts within uniform plastic) is therefore a poor probe of the effect, whereas a heterogeneous, statistically motivated power-law clutter phantom brings the effect immediately to light.

The observation is quantified in Fig. 3: the noise in water increases monotonically even in the region of low N_{proj}, whereas the noise in clutter is nonmonotonic and increases at low N_{proj} due to view sampling. The statistical error in the measurements was such that error bars were approximately the same size as the plot symbols and were therefore not shown for clarity. A different noise component emerges as N_{proj} increases, also evident in Figs. 2 and 3—a monotonic (approximately linear) increase in noise with increasing N_{proj}. Since D_{tot} is fixed, and increasing N_{proj} is associated with lower exposure per projection, X_{proj}, the culprit for the increase is clear: electronic noise. In both water and clutter, an increase in noise magnitude (with little or no change in noise texture) can be attributed to an increased contribution of electronic noise that adds to the NPS with a similar spatial-frequency characteristic as the quantum noise (i.e., midpass). As shown in Fig. 3, the effect is the same in water and clutter, the latter slightly elevated due to a slightly higher overall attenuation (lower transmission) of the clutter layer. The slope is related to the electronic noise level.

Figures 2 and 3 therefore give two distinct observations: (1) at fixed total dose in a uniform medium (water), noise increases monotonically with N_{proj} due to increasing contribution of electronic noise, whereas the underlying quantum noise component is constant, and the view aliasing noise component is not observed (since there is no structure in the object to alias) and (2) at fixed dose in a heterogeneous medium (clutter), noise increases at higher N_{proj} due to the effects just mentioned, and increases at lower N_{proj} due to view aliasing effects that arise from the clutter. In retrospect, the effects are intuitive, and a theoretical basis for such intuition is provided in Sec. 4.

Finally, there is a subtlety that becomes apparent in the NPS at low N_{proj}. As seen in the axial NPS of Fig. 4 for $N_{\text{proj}} = 40$, the NPS exhibits a discrete set of (20) vanes in the Fourier domain associated with the 40 backprojections. In that case, the angular increment is $\Delta\theta = 9^\circ$, and the second half of the scan is redundant such that backprojected rays overlie the same vanes in the Fourier domain. This effect is also related to the notion of 1/4-pixel offset for optimal sampling.[27] The suboptimal sampling becomes apparent at low N_{proj}. The observation prompted us to consider a separate scan acquired with $N_{\text{proj}} = 39$ ($\Delta\theta = 9.231^\circ$) such that the second half of the scan was not redundant. We hypothesized that the NPS would exhibit more complete filling of the Fourier domain but little or no change in the magnitude of the quantum noise (σ_Q), since the total dose was nearly unchanged (to one part in 40). The effect was confirmed as illustrated in Fig. 4, where a reduction by just one projection had a marked effect: the voxel noise in a uniform medium was essentially unchanged ($\sigma_{\text{vox}} = 0.0188$ and 0.0186 cm^{-1} for 39 and 40 projections, respectively, in agreement with the small change in dose of one part in 40); however, as hypothesized, reduction by one projection actually improved the voxel noise in a

heterogeneous medium ($\sigma_{\text{vox}} = 0.037$ and $0.038\ \text{cm}^{-1}$ for 39 and 40 projections, respectively) and the view aliasing streaks appear visibly reduced. It bears reiteration: the sampling *improved* despite having one fewer projection due to improved filling of the Fourier domain with nonoverlapping backprojections.

The observation of improved sampling for 39 versus 40 views is a subtlety of academic interest at extremes of angular undersampling and is only evident at very low values of N_{proj} where differences in Fourier domain filling are more appreciable and is unlikely to affect clinical image quality under conditions of more complete sampling. It is also most evident (or evident at all) near the center of reconstruction (~4 cm annular radius in the current study) and for systems with an extended SAD, where the discussion above regarding redundant rays is more consistent with a parallel beam approximation. The effect is reduced (or unobservable) at larger values of N_{proj}, at extended distances from the center of reconstruction, and for shorter SAD (high magnification), although the last two dependencies were not directly investigated in the current work. The effect could also warrant consideration in applications involving low-dose "sparse" CBCT data acquisition.[28,29]

4. AN ANALYTICAL BASIS FOR THE NOISE COMPONENTS

4.A. Three components of image noise

The trends evident in the measurements reported above can be understood in terms of three components of image noise—quantum noise, electronic noise, and view sampling—each described below in a simple analytical framework.

4.A.1. Quantum noise

Quantum noise refers to image fluctuations arising from the discrete nature of Poisson-distributed incident x-ray photons, the propagation of which in the image acquisition and reconstruction process is well described by cascaded systems analysis.[11] We follow the notation of Tward and Siewerdsen[11] and Gang *et al.*[12] in describing a cascade of gain, spreading, and sampling stages: (1) interaction of x rays in the converter; (2) conversion of x rays to secondary quanta (optical photons); (3) spatial spread of secondary quanta in the converter; (4) coupling of secondary quanta to the pixel aperture; (5) integration of secondary quanta by the pixel aperture; (6) detector readout (2D sampling); (7) addition of electronic noise; (8) normalization and logarithm of processed projection data; (9) application of the ramp filter; (10) application of the smoothing filter; (11) interpolation of detector pixel values; (12) backprojection; and (13) sampling of the 3D voxel grid. The 2D NPS describing quantum noise in a single projection image (i.e., up through stage 7) is[30]

$$\begin{aligned} S_7 &= \bar{q}_0 a_{\text{pd}}^4 \bar{g}_1 \bar{g}_2 \bar{g}_4 \left(1 + \bar{g}_4 P_K T_3^2\right) T_5^{2**}\text{III}_6 + S_{\text{add}} \\ &= S_7^Q + S_{\text{add}}, \end{aligned} \tag{4}$$

where $\bar{q}_0$ is the incident fluence, a_{pd} is the extent of the integrating aperture, the various $\bar{g}_i$ refer to the mean gain of stage i, P_K includes K-fluorescence effects in the x-ray converter,[25] T_i refers to the transfer function for stage i, III is the comb function representing the sampling distance, and S_{add} is the NPS associated with the readout electronics. For simplicity in the equations below, we will omit the sampling step—i.e., assume no aliasing from III_6, which is a fair approximation for band-limited indirect-detection FPDs. We will also ignore S_{add} for the moment (treated separately below) and focus on just the x-ray quantum noise.

The system MTF, T_{sys}, for backprojection over N_{proj} views is

$$\begin{aligned} T_{\text{sys}} = &\frac{\pi M}{N_{\text{proj}}} T_3 T_5 T_{10} T_{11} T_{12} \sum_{i=1}^{N_{\text{proj}}} d \\ &\times \text{sinc}\{d[f_x \cos(\theta_i) + f_y \sin(\theta_i)]\}, \end{aligned} \tag{5a}$$

where d is an arbitrary distance associated with the reconstruction FOV, and M is the system magnification (SDD/SAD). In the limit of complete sampling ($N_{\text{proj}} \to \infty$),

$$T_{\text{sys}}^{N_{\text{proj}}\to\infty} = T_3 T_5 T_{10} T_{11} T_{12} \frac{M}{f_r} \cong T_3 T_5 T_{11} T_{12} \tag{5b}$$

since T_{10} ($= \frac{f_r}{M}$, where $f_r = \sqrt{f_x^2 + f_y^2}$) and the backprojection operator perfectly cancel.

The resulting 3D NPS associated with quantum noise in the filtered backprojection image is

$$\begin{aligned} S_Q = &\frac{S_7^Q}{\left(\bar{q}_0 a_{\text{pd}}^2 \bar{g}_1 \bar{g}_2 \bar{g}_4\right)^2} T_{10}^2 T_{11}^2 T_{12}^2 \left[\left(\frac{1}{M}\right)^2 \left(\frac{M\pi}{N_{\text{proj}}}\right)^2 \sum_{i=1}^{N_{\text{proj}}} d \right. \\ &\left. \times \text{sinc}^2\{d[f_x \cos(\theta_i) + f_y \sin(\theta_i)]\}\right]. \end{aligned} \tag{6a}$$

In the limit of infinitely many projections,

$$\begin{aligned} S_Q^{N_{\text{proj}}\to\infty} &= \frac{S_7^Q}{\left(\bar{q}_0 a_{\text{pd}}^2 \bar{g}_1 \bar{g}_2 \bar{g}_4\right)^2} \left(\frac{f_r}{M}\right)^2 T_{11}^2 T_{12}^2 \\ &\quad \times \left[\left(\frac{1}{M}\right)^2 \left(\frac{M\pi}{N_{\text{proj}}}\right)^2 \frac{N_{\text{proj}}}{\pi} \frac{1}{f_r}\right] \\ &= \frac{\pi f_r}{N_{\text{proj}} M^2} \frac{S_7^Q}{\left(\bar{q}_0 a_{\text{pd}}^2 \bar{g}_1 \bar{g}_2 \bar{g}_4\right)^2} T_{11}^2 T_{12}^2. \end{aligned} \tag{6b}$$

The magnitude of quantum noise is

$$\sigma_Q^2 = \iiint S_Q(f_x, f_y, f_z) df_x df_y df_z. \tag{6c}$$

Equation (6b) reflects the midpass characteristic of the 3D NPS described early in the context of transaxial CT by Hanson[31] and Wagner *et al.*[32] As shown in Tward *et al.*,[11,12] carrying through the triple integral also reproduces the classic relationship of noise, dose, and spatial resolution as described by Barrett *et al.*[33]—i.e., the variance is inversely proportional to dose, slice thickness, etc.—but here accounting for the various nonidealities of the FPD imaging chain.

4.A.2. Electronic noise

Next, we consider the electronic readout noise introduced at stage 7, with NPS assumed to be uncorrelated

$$S_{\text{add}} = a_{\text{pd}}^2 \sigma_{\text{add}}^2, \tag{7}$$

where σ_{add} is the root mean square electronic noise. Propagating S_{add} through the process of filtered backprojection gives the 3D NPS associated with electronic noise

$$S_E = \frac{S_{\text{add}}}{\left(\bar{q}_0 a_{\text{pd}}^2 \bar{g}_1 \bar{g}_2 \bar{g}_4\right)^2} T_{10}^2 T_{11}^2 T_{12}^2 \left[\left(\frac{1}{M}\right)^2 \left(\frac{M\pi}{N_{\text{proj}}}\right)^2 \sum_{i=1}^{N_{\text{proj}}} d \times \text{sinc}^2\{d[f_x \cos(\theta_i) + f_y \sin(\theta_i)]\}\right]. \tag{8a}$$

In the limit of infinitely many projections,

$$S_E^{N_{\text{proj}}\to\infty} = \frac{\pi f_r}{N_{\text{proj}} M^2} \frac{S_{\text{add}}}{\left(\bar{q}_0 a_{\text{pd}}^2 \bar{g}_1 \bar{g}_2 \bar{g}_4\right)^2} T_{11}^2 T_{12}^2. \tag{8b}$$

Note that the 3D electronic NPS has a similar midpass spatial frequency dependence as the quantum noise—a ramp characteristic at low frequencies, peaking at midfrequencies, and rolling off due to apodization and interpolation. The electronic noise component of the CBCT image noise is

$$\sigma_E^2 = \iiint S_E(f_x, f_y, f_z) df_x df_y df_z \tag{8c}$$

and the noise associated with purely random processes of incident quanta and readout electronics is

$$\sigma_{Q+E}^2 = \iiint S_Q(f_x, f_y, f_z) + S_E(f_x, f_y, f_z) df_x df_y df_z. \tag{9}$$

4.A.3. View aliasing

Finally, we consider the effect of view sampling. As evident in Fig. 2, view sampling effects are only manifest in the presence of a heterogeneous object with structure subject to aliasing. A good example is the statistically motivated clutter phantom, designed to exhibit a symmetric 3D power-law NPS

$$S_{\text{obj}} = \frac{\kappa}{\left(\sqrt{f_x^2 + f_y^2 + f_z^2}\right)^\beta} = \frac{\kappa}{f^\beta} \tag{10a}$$

the reconstruction of which is subject to smoothing by the system MTF

$$S_B = S_{\text{obj}} T_{\text{sys}}^2. \tag{10b}$$

The NPS associated with view sampling effects is therefore

$$\begin{aligned} S_{\text{view}} &= S_B - S_B^{N_{\text{proj}}\to\infty} \\ &= \frac{\kappa}{f^\beta}\left[T_{\text{sys}}^2 - \left(T_{\text{sys}}^{N\text{proj}\to\infty}\right)^2\right] \\ &= \frac{\kappa}{f^\beta} T_3^2 T_5^2 T_{10}^2 T_{11}^2 T_{12}^2 \\ &\times \left[\left(\frac{\pi M}{N_{\text{proj}}}\right)^2 \left(\sum_{i=1}^{N_{\text{proj}}} d \,\text{sinc}\{d[f_x \cos(\theta_i) + f_y \sin(\theta_i)]\}\right)^2 - \frac{M^2}{f_r^2}\right]. \end{aligned} \tag{11a}$$

Note the spatial-frequency content of S_{view}: the term out front carries the low-frequency characteristic of the object ($1/f^\beta$) apodized by the various transfer functions in the acquisition and reconstruction process; the term in brackets goes as $\sim[\text{sinc}^2(f) - 1/f^2]$, which itself is low- to midpass; and there is an approximate $1/N_{\text{proj}}^2$ dependence. The resulting S_{view} is therefore a combination of low-frequency clutter-like noise and midfrequency correlated noise—i.e., streaks—blurred by the system MTF. The view aliasing noise component is simply

$$\sigma_{\text{view}}{}^2 = \iiint S_{view}(f_x, f_y, f_z) df_x df_y df. \tag{11b}$$

Numerical calculation of T_{sys} is prone to finite sampling effects where the summation of sinc functions does not nicely cancel out to $1/f$ even when N_{proj} is large. For purposes of numerical calculation, therefore, we defined a cutoff frequency as in Gang *et al.*,[12] below which the object is fully sampled with the transfer function $T_{\text{sys}}^{N_{\text{proj}}\to\infty}$, and above which has transfer function T_{sys}.

4.A.4. The total CBCT image noise

Considering the components of quantum noise, electronic noise, and view aliasing noise described above, the total image noise in CBCT is simply

$$\sigma_{\text{tot}}^2 = \iiint S_E(f_x, f_y, f_z) + S_Q(f_x, f_y, f_z) + S_{\text{view}}(f_x, f_y, f_z) df_x df_y df_z. \tag{12}$$

The magnitude and dependencies of each component is analyzed in Sec. 4.B, in each case relating back to the observations in Sec. 2. The parameters describing the imaging chain in Eqs. (4)–(12) were obtained as in previous work, derived theoretically from a model of the x-ray beam and detector design. The scintillator MTF (T_3) and detector electronic noise (σ_{add}) were estimated from measurements and taken as empirical input to the model. In the analysis of noise versus N_{proj} in Sec. 4.B, there was no fitting of theory to the measured results, and the level of agreement is simply that suggested from the cascaded systems model in Eqs. (4)–(12).

4.B. Magnitude and dependence of the noise components

The observed behavior of image noise versus N_{proj} (at constant D_{tot}) is described well by the analytical forms in Eqs. (4)–(12). Figure 5(a), for example, compares the measured voxel noise (in the clutter layer of the cylindrical phantom) in comparison to the prediction of Eq. (12) at $D_{\text{tot}} = 2$ and 8 mGy and at voxel size $b_{\text{vox}} = 0.22$ and 0.44 mm.

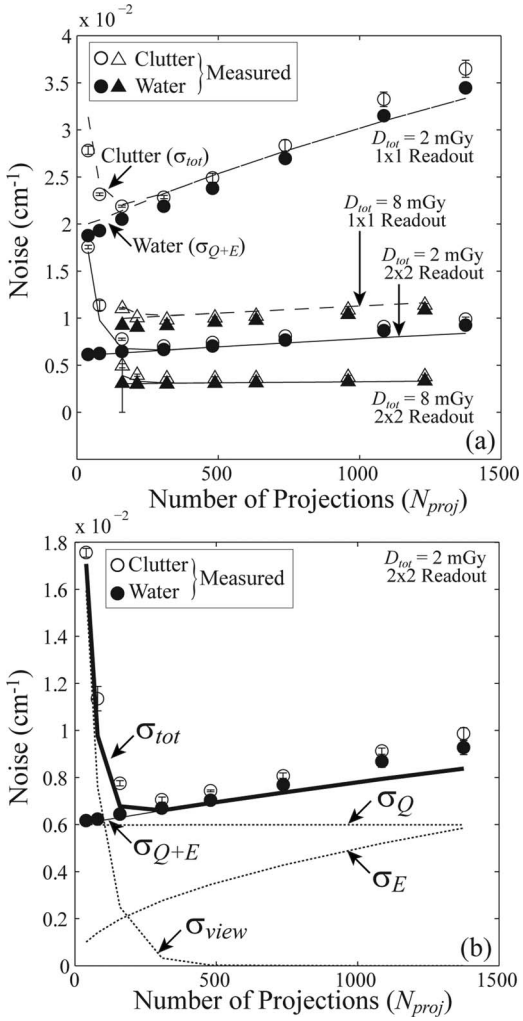

FIG. 5. Analytical model for CBCT noise versus N_{proj}. (a) Comparison of theory and measurement at various dose (2 and 8 mGy) and voxel size (0.22 and 0.44 mm). (b) Individual contributions of quantum noise (σ_Q), electronic noise (σ_E), and view sampling (σ_{view}) to the total voxel noise (σ_{tot}) as a function of N_{proj}.

Figure 5(b) breaks down one of the cases ($D_{\text{tot}} = 2$ mGy, $b_{\text{vox}} = 0.44$ mm) into the various noise components, where the behavior of σ_{tot} (and the optimum at $N_{\text{proj}} \sim 300$) is described well by a sum of components that are constant (σ_Q), monontonically increasing (σ_E), and monotonically decreasing (σ_{view}) as a function of N_{proj}.

The dependence of each noise component is further detailed in Fig. 6. The quantum noise (σ_Q) is seen to be independent of N_{proj} and varies in inverse proportion to the (square root of) total dose. On the other hand, the electronic noise (σ_E) increases as the (square root of) N_{proj} when dose per projection is fixed. View aliasing noise (σ_{view}) decreases approximately as ($1/N_{\text{proj}}$) and carries an explicit dependence on the value of κ and β in the power-law clutter model. The total noise (σ_{tot}) exhibits the now familiar nonmonotonic dependence on N_{proj}, and the optimal N_{proj} is seen to shift to higher values (or the optimum is lost altogether) as electronic noise is reduced—for example, σ_{tot} nearly independent of N_{proj} for $N_{\text{proj}} > 400$ and $\sigma_{\text{add}} < 2000$ e.

5. DISCUSSION AND CONCLUSIONS

This work revisits fairly fundamental considerations of CBCT image noise in experimental and theoretical analysis of the effect of the number of projections. It elucidates and quantifies trends that are intuitive in retrospect, while calling to light a number of less obvious effects with practical implications for system design and specification of scan protocols.

The measurements in Figs. 2–4 illustrate the tradeoffs among three noise components—quantum noise, electronics, noise, and view aliasing—under conditions of constant dose. While other work (e.g., Refs. 34 and 35) has investigated the question of noise and number of projections from various perspectives and applications (including, for example, tomosynthesis[34]), we are unaware of a study that so clearly illustrates the distinct contributions of each noise component at fixed total dose. The (perhaps surprising) appearance of a "sweet spot" (minimum) in the analysis of noise versus N_{proj} is intriguing, and it certainly defies the naïve logic of the rule of thumb expressed in Eq. (1). That rule of thumb, of course, is based on an oversimplified argument of sampling and spatial resolution, implying simply that more projections is better; however, the noise tells a different story, revealing an "optimal" N_{proj} that minimizes the contributions of electronic noise and view aliasing relative to the underlying (constant) quantum noise. Perhaps of no surprise to experimentalists at work in CBCT system development over the last decade, the optimum resides in a region about $N_{\text{proj}} \sim 300$, nearly an order of magnitude below that implied by Eq. (1).

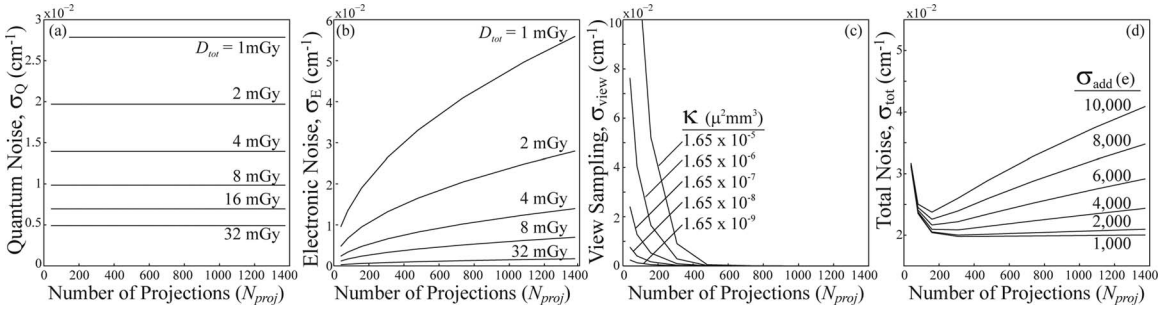

FIG. 6. Analysis of each noise component as a function of N_{proj}. (a) Quantum noise (σ_Q) evaluated at various levels of D_{tot}. (b) Electronic noise (σ_E) at various levels of D_{tot}. (c) View aliasing noise (σ_{view}) at various levels of the power-law magnitude κ. (d) Total voxel noise (σ_{tot}) at various levels of electronics noise.

The existence of the optimum owes directly to the relatively high level of electronic noise in FPDs, and for systems with higher performance detectors (i.e., lower readout noise relative to system gain), the optimum shifts to a higher number of projections and is eventually lost [Fig. 6(d)] such that a greater number of projections monotonically reduces image noise.

The position of the sweet spot is not a general result, and the dependence associated with any particular CBCT system is expected to depend on system configuration—most notably, the system geometry, choice of FPD, mode of operation, binning, and level of electronics noise. The theoretical analysis detailed in Sec. 4 provides a general framework for understanding such dependencies. The "optimal" N_{proj} increases as the electronic noise decreases, the total dose increases, and the voxel size increases. For sufficiently low electronic noise (and/or high dose or large voxels), the total noise reduces, the minimum in the plot of noise versus N_{proj} shifts ever more to the right, and the choice of N_{proj} falls to practical considerations of frame rate, scan speed, and the amount of projection data to transfer and reconstruct.

The experiments and imaging bench of Fig. 1 involved pulsed exposure "step-and-shoot" CBCT acquisition, thereby minimizing the potential influence of rotation (azimuthal blur) during x-ray exposure. Systems with differing pulse rate and detector readout rate can be expected to demonstrate a different dependence of noise on the number of views. For example, in CBCT systems employing continuous x-ray exposure during rotation, such an effect has been observed to impart a significant component of the MTF.[36] In the context of the work reported here, such azimuthal blur is anticipated to reduce view aliasing effects as well as stochastic quantum noise in a manner analogous to other sources of blur and correlation. As evident in both the experimental and theoretical results above, factors that reduce noise {e.g., increased D_{tot} [Figs. 3, 5(a), 6(a), and 6(b)], reduced σ_{add} [Fig. 6(d)], and increased pixel binning or voxel size [Figs. 3 and 5(a)]} tend to shift the "optimal" number of projections to higher values of N_{proj}.

Although beyond the scope of the current work, the best choice in N_{proj} also likely depends on the choice of reconstruction filter (smoother filters providing tolerance in N_{proj} analogous to increased dose or reduced electronic noise) and—almost certainly—depends on the choice of reconstruction algorithm, with statistical model-based methods providing a greater degree of robustness against sampling effects than filtered backprojection.[28,29] The work could certainly also be extended to task-based performance analysis (e.g., calculation of task-based detectability index as a function of N_{proj}), which is very much within the capacity of the framework detailed in Sec. 4; however, the purpose of the current work was to elucidate the fundamental components underlying image noise, and extension to task-based analysis and optimization is left to future work in the context of specific systems and applications.

The experiments also demonstrate a number of less obvious considerations with respect to sampling. The first is evident upon close inspection of the uniform and heterogeneous regions of the phantom imaged as a function of N_{proj} as in Fig. 2. The effect of a finite number of projections (i.e., noise associated with view sampling) is not well appreciated in a uniform medium; rather, view sampling is only evident when there is heterogeneous structure present in the image. The effect is most obvious for $N_{\text{proj}} < 200$ (the left-most portion of the curves in Fig. 3), where the increase in noise is entirely attributable to view sampling of object clutter (whereas the quantum and electronics noise measured in water are immune to such sampling effects). The observation is roughly consistent with findings from Zhao *et al.*,[37] who observed streaks in the NPS when angular separation between projections exceeded $\sim 2^\circ$. Phantoms presenting a uniform medium (or a simple arrangement of contrast inserts as in the ACR phantom, for example) are not well suited to probing the effect of view sampling under such conditions of few projection views. "Clutter phantoms"—popular in the last decade for simulating the anatomical power spectrum in applications such as breast CBCT (Refs. 38–40)—are considerably better suited to such measurement, and a collection of spheres of varying diameter and contrast [providing an approximation to noise of the form $1/f^3$ associated with a self-similar object (3D fractal)] was shown to provide a good, statistically motivated phantom for physically probing such sampling effects.[12]

Further consideration involves the effect of redundant rays on the noise and NPS as shown in Fig. 4. Especially under conditions of few projection views (N_{proj} below the "sweet spot"), N_{proj} should be selected to avoid redundant views (i.e., views separated by $\Delta\theta = 180^\circ$). Such redundant rays have little or no effect on quantum and electronics noise (which depend only on the total number of quanta presented to the imaging system), but they result in undersampling of the object (increase in σ_{view}) that is obvious in the NPS and carries a strong increase in view sampling as evident in the clutter images of Fig. 4 (but not in the corresponding water images). The sparsity of vanes in the NPS (i.e., poor filling of the Fourier domain) is absolved by using a number of projections and angular increment that do not evenly divide with redundant backprojections over the second half of the data. The effect is stronger in scenarios more closely approximating a parallel beam assumption (e.g., near the center of reconstruction and systems with an extended SAD and low magnification) and may be important to consider in applications involving sparse data acquisition as a means to reduce radiation dose and/or reduce computational load or reconstruction time.[28,29]

In summary, a common question in CBCT system design and operation was entertained using both experimentation and theory. The experiment elucidated and quantified the tradeoffs among quantum noise, electronics noise, and view aliasing as a function of the number of projections—particularly highlighting the importance of a heterogeneous object (e.g., a statistically motivated "clutter" phantom) in investigating such effects. The theoretical analysis provided an analytical foundation that agreed with the observed effects. Such methods may be potentially useful in designing and operating new CBCT systems for a particular application, can be extended to applications such as limited angle tomosynthesis, hold

implications for CBCT image reconstruction from sparse projection data, and could be helpful in understanding image quality effects among scan protocols on clinical CBCT scanners in applications ranging from breast and maxillofacial imaging to image-guided radiotherapy.

ACKNOWLEDGMENTS

Authors Z. Zhao and G. J. Gang contributed equally as first authors of this work. The research was supported by NIH Grant No. 2R01-CA-112163. Z. Zhao was supported in part by a scholarship from Tianjin University. The authors extend their gratitude to J. W. Stayman and W. Zbijewski (Johns Hopkins University) for assistance with experiments and image quality analysis.

[a]Author to whom correspondence should be addressed. Electronic mail: jeff.siewerdsen@jhu.edu; Telephone: 443-287-6269.

[1]J. M. Boone and K. K. Lindfors, "Breast CT: Potential for breast cancer screening and diagnosis," Future Oncol. **2**(3), 351–356 (2006).
[2]A. O'Connell, D. L. Conover, Y. Zhang, P. Seifert, W. Logan-Young, C.-F. L. Lin, L. Sahler, and R. Ning, "Cone-beam CT for breast imaging: Radiation dose, breast coverage, and image quality," Am. J. Roentgenol. **195**(2), 496–509 (2010).
[3]W. Zbijewski, P. De Jean, P. Prakash, Y. Ding, J. Stayman, N. Packard, R. Senn, D. Yang, J. Yorkston, and A. Machado, "A dedicated cone-beam CT system for musculoskeletal extremities imaging: Design, optimization, and initial performance characterization," Med. Phys. **38**, 4700–4713 (2011).
[4]A. C. Miracle and S. K. Mukherji, "Conebeam CT of the head and neck, Part 2: Clinical applications," Am. J. Neuroradiol. **30**(7), 1285–1292 (2009).
[5]J. H. Siewerdsen, "Cone-beam CT with a flat-panel detector: From image science to image-guided surgery," Nucl. Instrum. Methods Phys. Res. A **648**(1), S241–S250 (2011).
[6]J. H. Siewerdsen, D. J. Moseley, S. Burch, S. K. Bisland, A. Bogaards, B. C. Wilson, and D. A. Jaffray, "Volume CT with a flat-panel detector on a mobile, isocentric C-arm: Pre-clinical investigation in guidance of minimally invasive surgery," Med. Phys. **32**(1), 241–254 (2005).
[7]D. A. Jaffray, J. H. Siewerdsen, J. W. Wong, and A. A. Martinez, "Flat-panel cone-beam computed tomography for image-guided radiation therapy," Int. J. Radiat. Oncol., Biol., Phys. **53**(5), 1337–1349 (2002).
[8]R. D. Brooks, G. H. Glover, A. J. Talbert, R. L. Eisner, and F. A. DiBianca, "Aliasing: A source of streaks in computed tomograms," J. Comput. Assist. Tomogr. **3**(4), 511–518 (1979).
[9]P. M. Joseph, "The influence of gantry geometry on aliasing and other geometry dependent errors," IEEE Trans. Nucl. Sci. **7**, 1104–1111 (1980).
[10]P. M. Joseph, R. D. Spital, and C. D. Stockham, "The effects of sampling on CT images," Comput. Tomogr. **4**, 189–206 (1980).
[11]D. J. Tward and J. H. Siewerdsen, "Cascaded systems analysis of the 3D noise transfer characteristics of flat-panel cone-beam CT," Med. Phys. **35**(12), 5510–5529 (2008).
[12]G. J. Gang, D. J. Tward, J. Lee, and J. H. Siewerdsen, "Anatomical background and generalized detectability in tomosynthesis and cone-beam CT," Med. Phys. **37**(5), 1948–1965 (2010).
[13]J. M. Boone, T. R. Nelson, K. K. Lindfors, and J. A. Seibert, "Dedicated breast CT: Radiation dose and image quality evaluation," Radiology **221**(3), 657–667 (2001).
[14]X. Gong, S. J. Glick, B. Liu, A. A. Vedula, and S. Thacker, "A computer simulation study comparing lesion detection accuracy with digital mammography, breast tomosynthesis, and cone-beam CT breast imaging," Med. Phys. **33**(4), 1041–1052 (2006).
[15]R. Fahrig, R. Dixon, T. Payne, R. L. Morin, A. Ganguly, and N. Strobel, "Dose and image quality for a cone-beam C-arm CT system," Med. Phys. **33**(12), 4541–4550 (2006).
[16]C. J. Lai, C. C. Shaw, L. Chen, M. C. Altunbas, X. Liu, T. Han, T. Wang, W. T. Yang, G. J. Whitman, and S. J. Tu, "Visibility of microcalcification in cone beam breast CT: Effects of X-ray tube voltage and radiation dose," Med. Phys. **34**(7), 2995–3004 (2007).
[17]K. G. Metheany, C. K. Abbey, N. Packard, and J. M. Boone, "Characterizing anatomical variability in breast CT images," Med. Phys. **35**(10), 4685–4694 (2008).
[18]N. J. Packard, C. K. Abbey, K. Yang, and J. M. Boone, "Effect of slice thickness on detectability in breast CT using a prewhitened matched filter and simulated mass lesions," Med. Phys. **39**(4), 1818–1830 (2012).
[19]L. Chen, C. K. Abbey, and J. M. Boone, "Association between power law coefficients of the anatomical noise power spectrum and lesion detectability in breast imaging modalities," Phys. Med. Biol. **58**(6), 1663–1681 (2013).
[20]Y. Cho, D. J. Moseley, J. H. Siewerdsen, and D. A. Jaffray, "Accurate technique for complete geometric calibration of cone-beam computed tomography systems," Med. Phys. **32**(4), 968–983 (2005).
[21]L. A. Feldkamp, L. C. Davis, and J. W. Kress, "Practical cone-beam algorithm," J. Opt. Soc. Am. A **1**(6), 612–619 (1984).
[22]J. H. Siewerdsen, A. M. Waese, D. J. Moseley, S. Richard, and D. A. Jaffray, "Spektr: A computational tool for x-ray spectral analysis and imaging system optimization," Med. Phys. **31**(11), 3057–3067 (2004).
[23]A. E. Burgess, "Mammographic structure: Data preparation and spatial statistics analysis," Medical Imaging'99. International Society for Optics and Photonics **3661**, 642–653 (1999).
[24]J. J. Heine, S. R. Deans, R. P. Velthuizen, and L. P. Clarke, "On the statistical nature of mammograms," Med. Phys. **26**, 2254–2265 (1999).
[25]S. Richard, J. H. Siewerdsen, D. A. Jaffray, D. J. Moseley, and B. Bakhtiar, "Generalized DQE analysis of radiographic and dual-energy imaging using flat-panel detectors," Med. Phys. **32**(5), 1397–1413 (2005).
[26]S. Yoon, J. G. Gang, D. J. Tward, J. H. Siewerdsen, and R. Fahrig, "Analysis of lung nodule detectability and anatomical clutter in tomosynthesis imaging of the chest," Proc. SPIE **7258**(1), 72581M (2009).
[27]T. Peters and R. Lewitt, "Computed tomography with fan beam geometry," J. Comput. Assist. Tomogr. **1**(4), 429–436 (1977).
[28]G. H. Chen, J. Tang, and S. Leng, "Prior image constrained compressed sensing (PICCS): A method to accurately reconstruct dynamic CT images from highly undersampled projection data sets," Med. Phys. **35**(2), 660–663 (2008).
[29]J. Bian, J. H. Siewerdsen, X. Han, E. Y. Sidky, J. L. Prince, C. A. Pelizzari, and X. Pan, "Evaluation of sparse-view reconstruction from flat-panel-detector cone-beam CT," Phys. Med. Biol. **55**(22), 6575–6599 (2010).
[30]J. H. Siewerdsen, L. E. Antonuk, Y. ElMohri, J. Yorkston, W. Huang, J. M. Boudry, and I. A. Cunningham, "Empirical and theoretical investigation of the noise performance of indirect detection, active matrix flat-panel imagers (AMFPIs) for diagnostic radiology," Med. Phys. **24**(1), 71–89 (1997).
[31]K. M. Hanson, "Detectability in computed tomographic images," Med. Phys. **6**(5), 441–451 (1979).
[32]R. F. Wagner, D. G. Brown, and M. S. Pastel, "Application of information theory to the assessment of computed tomography," Med. Phys. **6**, 83–94 (1979).
[33]H. Barrett, S. Gordon, and R. Hershel, "Statistical limitations in transaxial tomography," Comput. Biol. Med. **6**(4), 307–323 (1976).
[34]I. Sechopoulos, "A review of breast tomosynthesis. Part I. The image acquisition process," Med. Phys. **40**, 014301 (12pp.) (2013).
[35]A. Van Daatselaar, P. Van der Stelt, and J. Weenen, "Effect of number of projections on image quality of local CT," Dentomaxillofac. Radiol. **33**(6), 361–369 (2004).
[36]A. L. Kwan, J. M. Boone, K. Yang, and S. Y. Huang, "Evaluation of the spatial resolution characteristics of a cone-beam breast CT scanner," Med. Phys. **34**(1), 275–281 (2007).
[37]B. Zhao and W. Zhao, "Three-dimensional linear system analysis for breast tomosynthesis," Med. Phys. **35**(12), 5219–5232 (2008).
[38]P. R. Bakic, A. K. Carton, D. Kontos, C. Zhang, A. B. Troxel, and A. D. Maidment, "Breast percent density: Estimation on digital mammograms and central tomosynthesis projections," Radiology **252**(1), 40–49 (2009).
[39]B. Chen, J. Shorey, R. S. Saunders, Jr., S. Richard, J. Thompson, L. W. Nolte, and E. Samei, "An anthropomorphic breast model for breast imaging simulation and optimization," Acad. Radiol. **18**(5), 536–546 (2011).
[40]B. A. Lau, I. Reiser, R. M. Nishikawa, and P. R. Bakic, "A statistically defined anthropomorphic software breast phantom," Med. Phys. **39**(6), 3375–3385 (2012).